Title
Actin and dynamin2 dynamics and interplay during clathrin-mediated endocytosis.

Journal
The Journal of cell biology, 205(5)

ISSN
0021-9525

Authors
Grassart, Alexandre
Cheng, Aaron T
Hong, Sun Hae
et al.

Publication Date
2014-06-01

DOI
10.1083/jcb.201403041

Peer reviewed

Actin and dynamin2 dynamics and interplay during clathrin-mediated endocytosis

Alexandre Grassart,[1] Aaron T. Cheng,[1] Sun Hae Hong,[1] Fan Zhang,[2] Nathan Zenzer,[2] Yongmei Feng,[2] David M. Briner,[2] Gregory D. Davis,[2] Dmitry Malkov,[2] and David G. Drubin[1]

[1]Department of Molecular and Cell Biology, University of California, Berkeley, Berkeley, CA 94720
[2]Cell-Based Assays/Reporter Cell Lines, Sigma-Aldrich Research Biotech, St. Louis, MO 63103

Clathrin-mediated endocytosis (CME) involves the recruitment of numerous proteins to sites on the plasma membrane with prescribed timing to mediate specific stages of the process. However, how choreographed recruitment and function of specific proteins during CME is achieved remains unclear. Using genome editing to express fluorescent fusion proteins at native levels and live-cell imaging with single-molecule sensitivity, we explored dynamin2 stoichiometry, dynamics, and functional interdependency with actin. Our quantitative analyses revealed heterogeneity in the timing of the early phase of CME, with transient recruitment of 2–4 molecules of dynamin2. In contrast, considerable regularity characterized the final 20 s of CME, during which ∼26 molecules of dynamin2, sufficient to make one ring around the vesicle neck, were typically recruited. Actin assembly generally preceded dynamin2 recruitment during the late phases of CME, and promoted dynamin recruitment. Collectively, our results demonstrate precise temporal and quantitative regulation of the dynamin2 recruitment influenced by actin polymerization.

Introduction

Clathrin-mediated endocytosis (CME) is a key process in all eukaryotes by which portions of the plasma membrane, along with extracellular material, are internalized (McMahon and Boucrot, 2011). The recruitment and the cooperative actions of clathrin coat proteins together with cargo, adaptors, and over 40 accessory proteins mediate the formation of membrane invaginations called clathrin-coated pits (CCPs). Eventually, a new vesicle is formed. Live-cell imaging studies provided important details about the spatial and temporal organization of the factors involved in this sequence of events (Gaidarov et al., 1999; Ehrlich et al., 2004; Kaksonen et al., 2005; Taylor et al., 2011). However, how this ordered orchestration takes place is poorly understood. Live-cell imaging in mammalian cells revealed high heterogeneity in clathrin-mediated endocytosis dynamics and vesicle formation efficiency at the plasma membrane (Loerke et al., 2009). The extent to which this variability reflects technical limitations versus genuine molecular differences is an important issue that remains to be settled. In addition, full mechanistic understanding of CME will require accurate measurement of endocytic protein stoichiometry. Recently, in fission yeast the combination of quantitative imaging with genomic integration, which enables fluorescent fusion derivatives of native proteins to be expressed at physiological levels, has proved very powerful for determining the stoichiometry of proteins in dynamic cellular structures (Wu and Pollard, 2005). With the recent revolution in genome editing (Doyon et al., 2011; Gibson et al., 2013), similar analyses should be feasible in mammalian cells.

In mammalian cells, dynamin2, a GTPase responsible for vesicle scission, has been extensively studied (Ferguson and De Camilli, 2012). Structural studies suggest that ∼13 dynamin dimers can form a helical supra-structure that will encircle the neck of a budding vesicle (Hinshaw and Schmid, 1995; Chappie et al., 2011; Faelber et al., 2011). By varying parameters such as protein concentration or membrane tension in vitro, several models for dynamin's vesicle scission mechanism have been proposed (Morlot and Roux, 2013). However, testing how these models translate in vivo is challenging. Live-cell imaging revealed

A. Grassart and A.T. Cheng contributed equally to this paper.

Correspondence to David G. Drubin: drubin@berkeley.edu

Abbreviations used in this paper: ACTB, β-actin; CCP, clathrin-coated pit; CCS, clathrin-coated structure; CME, clathrin-mediated endocytosis; CLTA, clathrin light chain A; DNM2, dynamin2; TIRF, total internal reflection fluorescence; ZFN, zinc-finger nuclease.

The Rockefeller University Press $30.00
J. Cell Biol. Vol. 205 No. 5 721–735
www.jcb.org/cgi/doi/10.1083/jcb.201403041

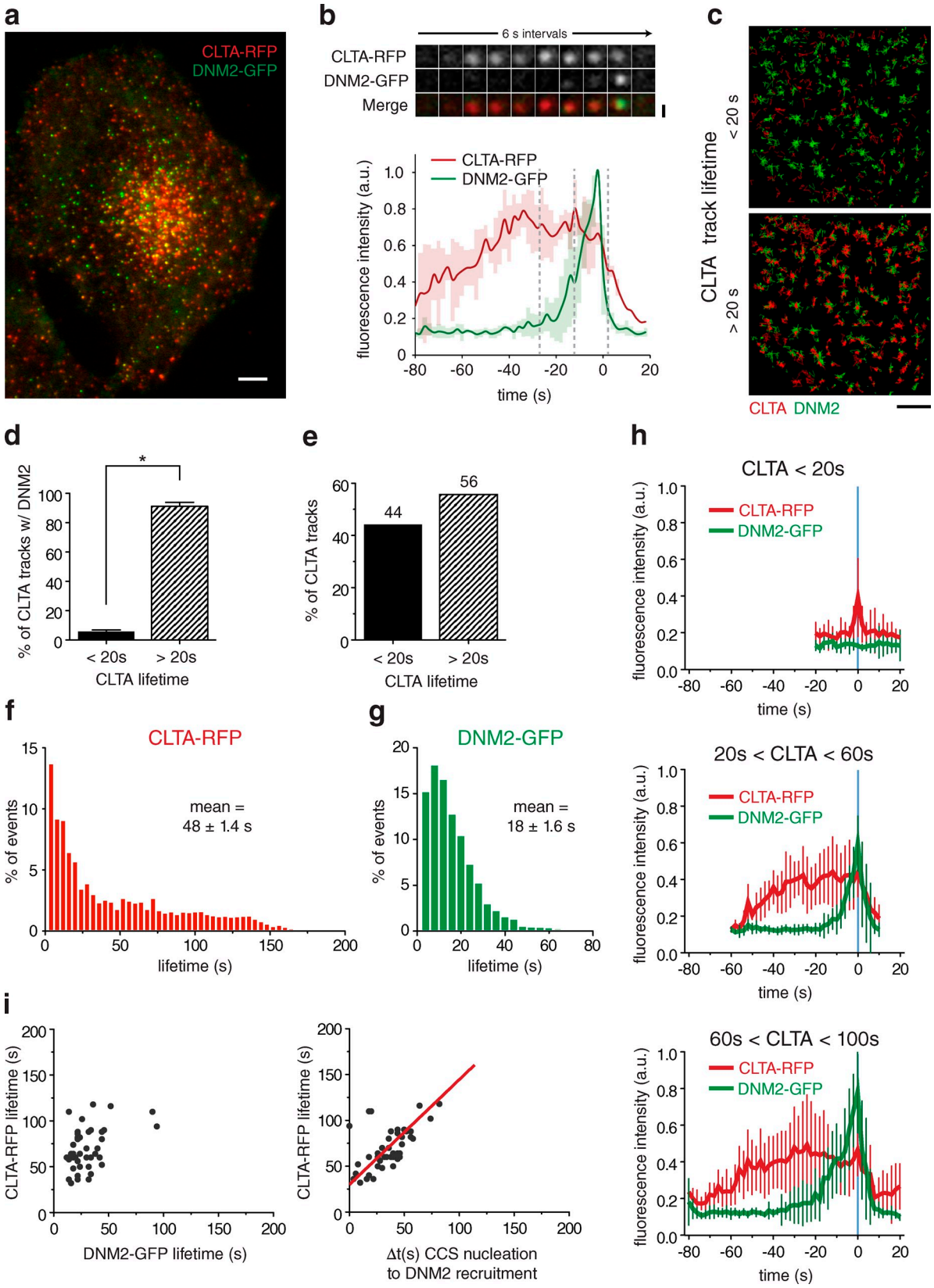

Figure 1. **Dynamin2 recruitment to endocytic sites.** (a) TIRF microscopy image of a representative SK-MEL-2 hCLTA^{EN}/hDNM2^{EN} cell expressing both CLTA-RFP and DNM2-EGFP. Bar, 5 µm. (b) Representative montage (top) and average fluorescence intensity profile (bottom) for endocytic events (tracks = 42; *n* = 3 cells). Shaded bars represent SEM. Bar, 500 nm. (c) Representative overlays of a cropped region (10 × 10 µm) of cell imaged for 120 frames (240 s) in which all DNM2-GFP tracks (in green) are displayed (identically in both images), whereas CLTA-RFP tracks (in red) are segmented by lifetime and displayed as tracks <20 s or >20 s on top or bottom images, respectively. Bar, 2 µm. (d) The mean percentage of CLTA punctae (±SEM), of <20 s or >20 s duration, that display robust dynamin recruitment (tracks = 903 or 815, respectively; *n* = 5 cells; *, P < 0.0001). (e) The percentage of CLTA punctae

that peak dynamin2 recruitment occurs near the end of the clathrin lifetime (i.e., the moment of vesicle scission; Merrifield et al., 2002; Soulet et al., 2005; Taylor et al., 2011). Interestingly, it has also been reported that a lower level of dynamin2 recruitment precedes this burst (Taylor et al., 2011; Aguet et al., 2013). So far, the dynamin2 kinetic recruitment signature during this "early" stage remains poorly defined. Dynamin2 intensity at sites of CME was reported to flicker during the early stage, and its lifetime to vary dramatically from several seconds to a few minutes (Mattheyses et al., 2011; Taylor et al., 2011). The early population of dynamin2 has been suggested to regulate CCP lifetime and maturation (Sever et al., 2000; Damke et al., 2001; Loerke et al., 2009; Taylor et al., 2012), and was suggested to function in a checkpoint that monitors CCP maturation (Loerke et al., 2009). Assessing such possible dynamin2 functions requires accurate analysis of recruitment dynamics and the number of molecules recruited.

A growing body of work supports a role for the actin cytoskeleton in CME. A recent study established that membrane tension is an important determinant of the CME dependency on actin in mammalian cells (Boulant et al., 2011). This work may partially explain previous pharmacological studies reporting varying degrees of cargo uptake dependency on actin assembly (Lamaze et al., 1997; Fujimoto et al., 2000; Saffarian et al., 2009). However, important unanswered questions remain about the regularity of actin recruitment, when actin assembles at CME sites, how actin is recruited, and how actin recruitment affects subsequent events. Interestingly, many actin regulators interact directly or indirectly with dynamin2, suggesting that actin and dynamin cooperate during CME, and reinforcing the conclusion that actin plays a role during the late stages of CME (Menon and Schafer, 2013). Recently, such a model has been reinforced by discovery of a feedback loop between dynamin and actin to promote vesicle scission (Taylor et al., 2012). Interestingly, dynamin1/2 double-knockout cells form tubules decorated with actin (Yarar et al., 2005; Ferguson et al., 2009). This observation strongly supports a role for actin before and independent of dynamin2 engagement. However, current live-cell imaging studies seem to contradict this model because actin polymerization was only detected during a time window shared with dynamin2 (Merrifield et al., 2002; Yarar et al., 2005; Saffarian et al., 2009). Because actin imaging is notoriously challenging, it is possible that actin is recruited before dynamin2 but was not detected (Collins et al., 2011). Importantly, simultaneous imaging of dynamin2 and actin has yet to be performed.

In the present study, we used the advantages of genome editing using zinc finger nucleases together with quantitative microscopy with single-molecule sensitivity to analyze the native dynamics of dynamin2 and its interplay with actin during CME.

Results

Analysis of dynamin2 dynamics during clathrin-mediated endocytosis

First, we sought to quantitatively analyze dynamin2 dynamics during CME. To do so, we used a genome-edited SK-MEL-2 cell line coexpressing C-terminal genomic fusions of Tag-RFP-t to clathrin light chain A (CLTA), and of enhanced green fluorescent protein (eGFP) to dynamin2 (DNM2; $hCLTA^{EN}$/$hDNM2^{EN}$, clone Ti13; Doyon et al., 2011). Use of these genome-edited cells provides several unique advantages. First, effects of dynamin overexpression such as cytotoxicity are avoided (Fish et al., 2000). Second, by not editing all alleles, potential effects of the fluorescent tags on CME dynamics are minimized (Doyon et al., 2011). Third, the stoichiometry of the core machinery remains unperturbed. Finally, integration of sequences encoding fluorescent tags at the native genomic loci via genome editing provides uniform fluorescent protein expression across the entire cell population, affording us the ability to perform unbiased, global analyses of protein recruitment and disassembly kinetics.

We analyzed CME dynamics in the genome-edited cells using total internal reflection fluorescence (TIRF) microscopy, which allowed high temporal and spatial resolution at the ventral face of the plasma membrane. At steady state, we observed a high degree of colocalization between DNM2-GFP and CLTA-RFP punctae, as described previously (Fig. 1 A; Doyon et al., 2011). By simultaneously imaging clathrin and dynamin2 in living cells, we observed that dynamin2 was recruited to clathrin punctae near the end of their lifetimes, consistent with dynamin's role in catalyzing membrane scission (Fig. 1 B). We analyzed dynamin's recruitment to clathrin punctae by collecting intensity traces for multiple CCPs using a time resolution of 2 s. The clathrin fluorescence followed a very similar profile to what was observed by others. Typically, clathrin intensity increased gradually and slowly, reached a plateau, and then quickly decreased. In addition, we observed significant detail in our analysis of dynamin2 dynamics. First, we observed that the majority of dynamin2 traces show similarity in duration and profile. In 90% of events, dynamin2 intensity increased once clathrin intensity plateaued. Infrequently (10% of events), dynamin2 recruitment started during the clathrin recruitment phase (Fig. S1 A). Despite this variation, averaging of multiple traces had only a limited effect on the dynamin2 signature (Fig. 1 B). Importantly, we could also observe some additional features common to all traces. First, we did not observe simultaneous initial recruitment of clathrin and dynamin2. Second, the maximum for clathrin assembly invariably precedes the maximum for dynamin2 recruitment. Finally, the dynamin2 intensity dropped dramatically over ∼4–6 s, ultimately returning to the pre-recruitment level. These observations suggest that timing of

having lifetimes <20 s or >20 s (tracks = 21,455; n = 5 cells). (f and g) Global lifetime distribution of CLTA-RFP and DNM2-GFP punctae (mean = 48 ± 1.4 s or 18 ± 1.6 s, respectively; tracks = 21,455 or 1,706, respectively; n = 5 or 3 cells, respectively). (h) Representative fluorescence intensity profiles of CLTA-RFP and DNM2-GFP for clathrin tracks <20 s (top), 20–60 s (middle), or 60–100 s (bottom). Blue line denotes time of maximum DNM2-GFP fluorescence (tracks = 10). (i) CLTA-RFP–DNM2-GFP punctae lifetime dot plot (left) and CLTA-RFP punctae lifetime relative to time from endocytic site initiation to maximum DNM2-GFP fluorescence. Each dot represents a single endocytic event (tracks analyzed = 46).

dynamin2 recruitment and assembly might be dependent on the passage of a certain threshold of CCP assembly or maturation.

Recently, dynamin has been proposed to control lifetimes of clathrin punctae in mammalian cells (Loerke et al., 2009). Therefore, we sought to determine under native expression conditions if dynamin dynamics are correlated with CCP lifetime. Using a semi-automatic tracking analysis, we measured the global lifetime distributions for clathrin and dynamin2 punctae. In contrast to the wide variance of clathrin lifetimes (Fig. 1 F), we found a considerably more limited dynamin2 lifetime distribution, with an average lifetime of 18 ± 1.6 s (Fig. 1 G). This result indicates that dynamin2 lifetime is independent of clathrin lifetime.

We next sought to determine whether the timing of dynamin2 recruitment to clathrin-coated structures (CCSs) depends on clathrin lifetimes. We observed that initial dynamin2 recruitment mostly occurs after the first 20 s of clathrin recruitment (Fig. 1 B). Interestingly, previous studies of clathrin lifetimes suggested that CCPs with lifetimes under 20 s are abortive (Ehrlich et al., 2004; Loerke et al., 2009). Because dynamin is required for scission events, we hypothesized that nonproductive events should be devoid of dynamin2. Therefore, we performed a global analysis, dividing clathrin punctae into two subpopulations using a threshold of a 20-s clathrin lifetime. In support of our hypothesis, dynamin punctae overwhelmingly (91 ± 2.7%) overlapped with clathrin punctae with lifetimes greater than 20 s, which comprised 56% of all clathrin punctae, but rarely (∼5.9 ± 1.1%) overlapped with punctae with shorter lifetimes (Fig. 1, C–E). These observations are in agreement with the previously posited hypothesis that short-lived clathrin punctae represent nonproductive events (Ehrlich et al., 2004; Loerke et al., 2009). Our results using simultaneous two-color imaging of tagged clathrin and dynamin2 expressed at endogenous levels support the conclusion that a transition occurs in the subset of clathrin structures with lifetimes greater than 20 s that allows them to become productive in vesicle formation.

We next determined whether dynamin2 exhibits different behavior at CCPs of different lifetimes, which would suggest that the dynamin2 recruitment profile is affected by or affects CCP maturation rates. Dynamin2 intensity profiles were determined for three subpopulations of CCPs based on their clathrin lifetimes (T_{CLC}): $T_{CLC} < 20$ s, 20 s $< T_{CLC} <$ 60 s, and 60 s $< T_{CLC} <$ 100 s (Fig. 1 H). Consistent with our analysis described above, we rarely detected dynamin2 in CCPs with lifetimes under 20 s. Dynamin2 profiles for the two other clathrin subpopulations revealed highly regular association/dissociation kinetics. Importantly, we did not observe a correlation between dynamin2 lifetimes and CCP lifetimes (Fig. 1 I). Accordingly, our analysis showed that for CCPs with longer lifetimes, dynamin2 was recruited later. This result establishes a strong association between dynamin2 recruitment timing and CCP lifetime (Fig. 1 I). Thus, these results demonstrate that the kinetics of the final stage of CME involving dynamin2 recruitment are highly regular. The regularity of dynamin2 dynamics revealed that clathrin-mediated endocytosis can be separated mechanistically into at least two distinct phases. The first phase, during which clathrin accumulates, is considerably variable in duration, whereas the subsequent phase, involving dynamin recruitment and function in scission, is highly regular.

Mechanism of dynamin2 recruitment and function

Understanding dynamin2's scission mechanism requires knowledge of the number of molecules present as a function of time. Previously, expression of fluorescent fusions of proteins expressed from their native promoters was shown to enable measurement of the number of molecules associated with specific structures in live yeast cells (Wu and Pollard, 2005; Sirotkin et al., 2010). Here, we decided to measure the number of dynamin2-GFP molecules at endocytic sites in live human cells. First, we used a genome-edited cell line in which all dynamin2 was expressed at the endogenous genomic loci from the natural promoter as GFP fusions (Doyon et al., 2011). Next, we calibrated our imaging system for the fluorescence of single GFP molecules as described previously (Fig. 2; Cocucci et al., 2012). Briefly, purified GFP molecules were allowed to coat coverslips at low density and were then imaged (Fig. 2, A–C). By analyzing the intensity distribution of the detected spots, we observed that most GFPs showed similar intensities (Fig. 2 D). To verify that the spots correspond to single molecules, we imaged our sample at a high frequency of 10 Hz and analyzed their intensity profiles over time. In a majority of cases, we observed that the intensity of an individual GFP spot decreased in an irreversible, single-step manner (Fig. 2 E). This observation validates our ability to detect and measure the intensity of single GFP molecules by TIRF. We then imaged dynamin2 under the same calibrated settings (Fig. 2 F). Finally, we determined the number of dynamin2 molecules over time using the established intensity standard. We observed that the brightest peak of dynamin2 corresponded to an average recruitment of ∼35 molecules (±13 molecules; Fig. 2 G). Based on recent structural analyses (Chappie et al., 2011; Faelber et al., 2011), our results indicate that sufficient dynamin2 is present at endocytic sites to form at least one full turn around a vesicle neck. Interestingly, in ∼56% of individual events, ∼26 ± 5 molecules of dynamin2 were recruited, sufficient to form no more than one turn around the vesicle neck (Fig. 2 H). In a minority of events, we observed that sufficient dynamin2 is recruited to assemble either 2 or 3 complete turns (44 ± 8 molecules and 77 ± 8 molecules, respectively; Fig. 2 H and Fig. S1, B and C). Therefore, our results indicate that under physiological conditions, only short dynamin2 helices are generated.

Previously, the role of dynamin catalytic activity and domains has been extensively investigated in vitro and in vivo. Using EM, it was observed that dynamin locked in the GTP-bound conformation forms membrane tubules decorated by dynamin helices (Takei et al., 1995). We used our quantitative approach to determine in living cells whether a similar enrichment of endogenous dynamin2 at endocytic sites could be detected. For this analysis, we directly targeted the dynamin2 GTPase domain with the inhibitor Dynasore (Macia et al., 2006) in our genome-edited cells. Although dynamin drugs can have

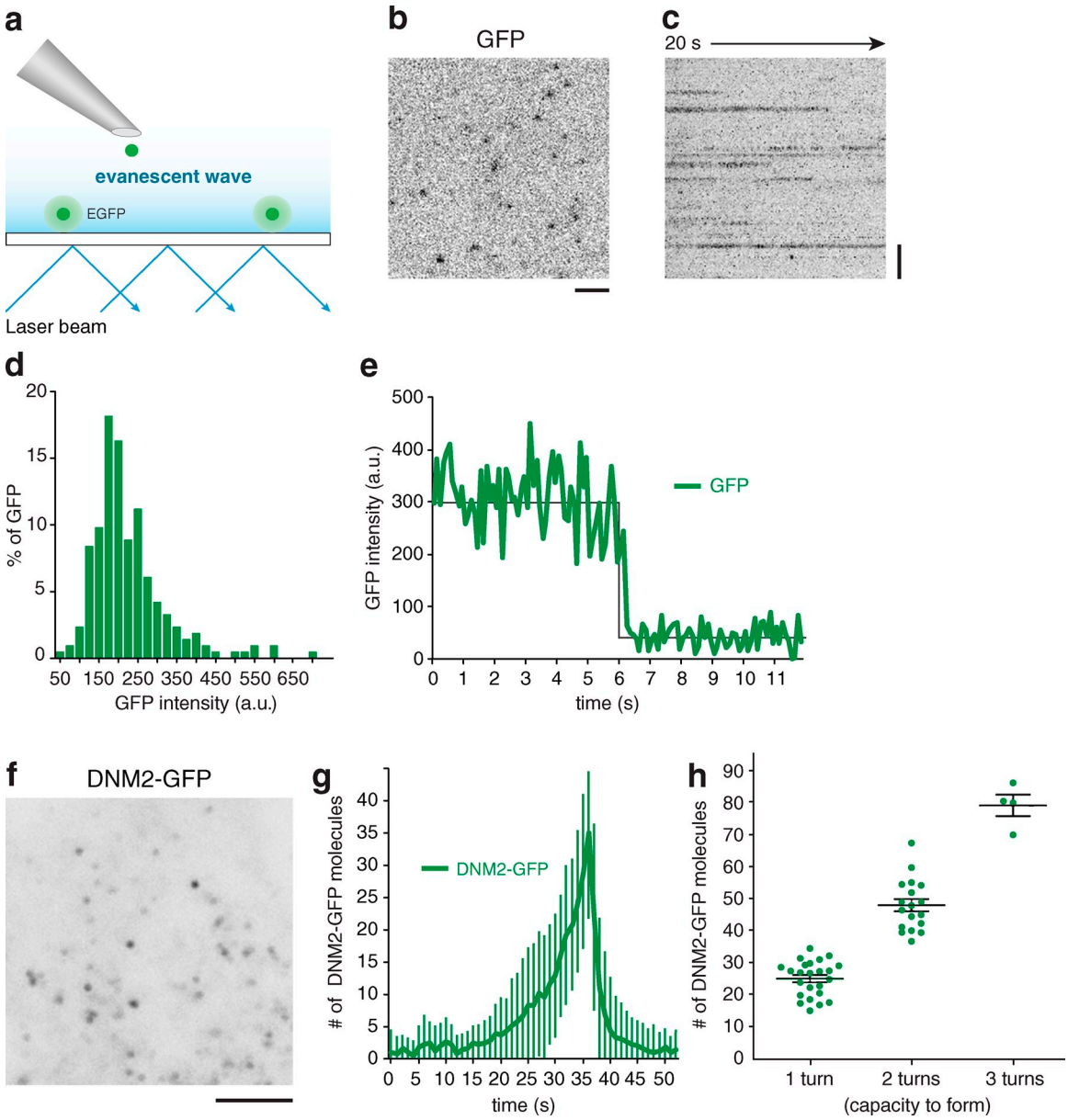

Figure 2. **Quantitation of dynamin2 recruitment to endocytic sites.** (a) Schematic representation of the TIRF imaging setup used for the experiments. This illustration shows that purified eGFP molecules were deposited at a low surface density on a polylysine-coated coverslip. After extensive washes, molecules were illuminated continuously with TIRF and recorded at a frequency of 10 Hz. (b) Frame from a TIRF acquisition time-series obtained using 100-ms exposures. The spots represent eGFP molecules. Bar, 1 µm. (c) Representative kymograph from a time-series of eGFP imaging. Bar, 1 µm. (d) Distribution of eGFP intensity measured (n = 215). (e) Representative fluorescence intensity trace corresponding to single bleaching step. (f) Frame from a TIRF acquisition time-series for a genome-edited DNM2$^{EN\text{-}all}$ SK-MEL-2 cell line endogenously expressing DNM2-GFP. Bar, 5 µm. (g) Average number of DNM2-GFP molecules recruited at the plasma membrane as a function of time (n = 40 endocytic sites in 3 cells). (h) Distribution of dynamin2 molecules in function of the theoretical capacity to form helices (n = 40 in 3 cells).

off-target effects (Park et al., 2013), our approach avoided perturbation of dynamin stoichiometry, which occurs during transient overexpression of dynamin mutants. Interestingly, we observed that dynamin2 molecules were recruited to endocytic sites over a longer than normal time and in higher than normal numbers in response to Dynasore (Fig. S3, A, C, D, E, and F). This elevated dynamin2 recruitment suggests formation of additional helices. Overall, our live-cell imaging and quantification results are congruent with those of previous EM studies (Takei et al., 1995).

Although the role of dynamin2's GTPase activity has been studied extensively, less is known about the function of its PH domain. Therefore, we tested its role by acutely inhibiting this domain using MiTMAB, a surface-active cationic amphiphilic compound (Quan et al., 2007). After 30 min of perfusion, we observed that endogenous dynamin2 was still recruited to the plasma membrane (Fig. S3 A). This result is in agreement with results of previous studies using transient overexpression of a dynamin PH domain mutant (Bethoney et al., 2009). Accordingly, we observed that an overexpressed PH mutant was still

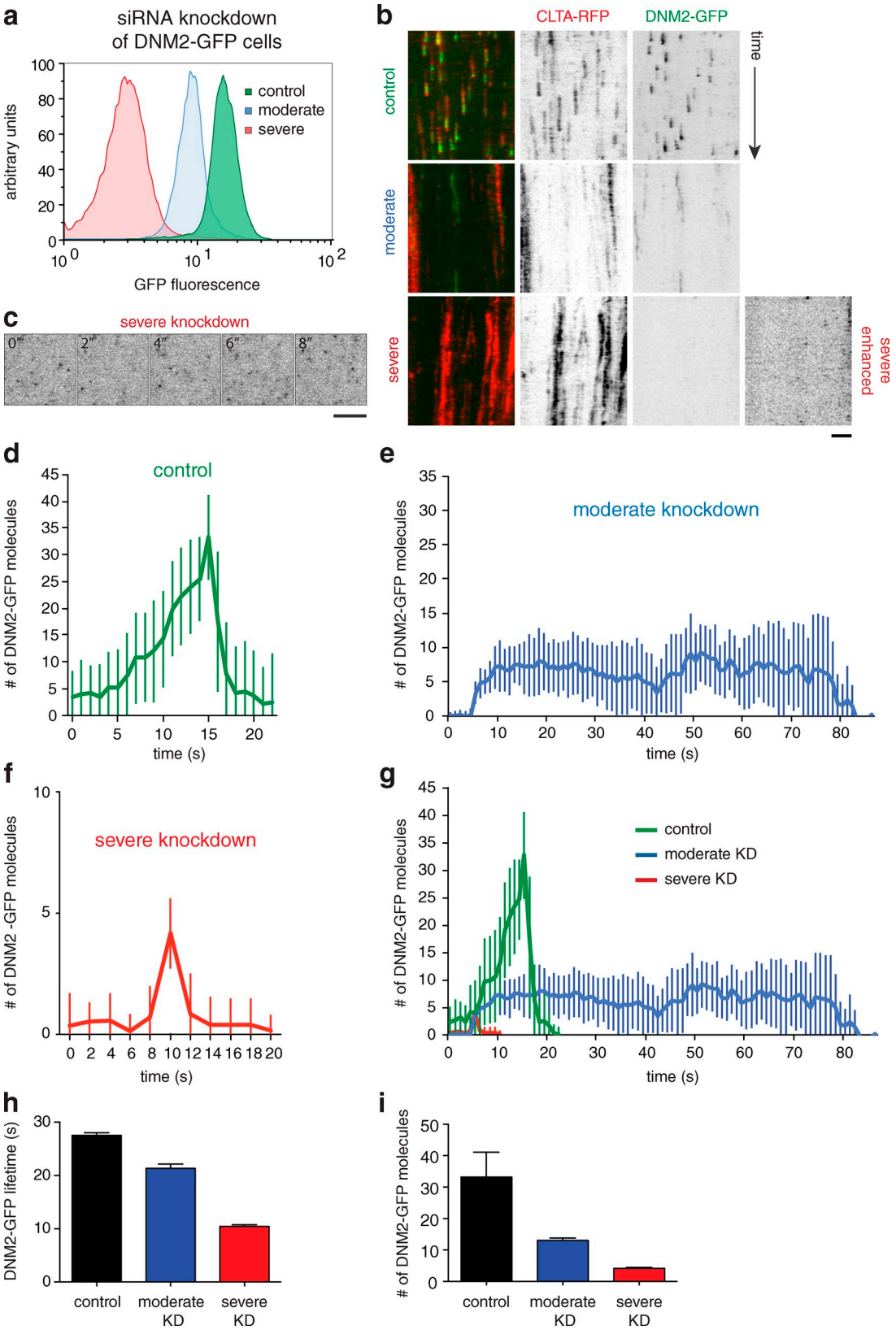

Figure 3. **Concentration dependence of dynamin2 recruitment to endocytic sites.** (a) Representative histogram plot of GFP fluorescence intensity for cell populations analyzed by FACS. Cells were subjected to treatment with mock siRNAs or siRNAs targeted to dynamin2, and were sorted 3 d after treatment by FACS for moderate or severe DNM2-GFP knockdown. For the experiment shown, number of events analyzed = 24,467 (control), 29,711 (moderate), and 16,286 (severe). (b) Kymograph analysis of representative cells subjected to varying degrees (control, moderate, or severe) of DNM2-GFP depletion. CLTA-RFP is red and DNM2-GFP is green. Enhanced = increased contrast image for severe depletion condition. Time, 180 s. Bar, 2 µm. (c) Representative montage of a region of a cell subjected to severe dynamin2 depletion. DNM2-GFP is shown. Contrast of images was enhanced for better visualization.

recruited to endocytic sites (Fig. S4 D). In contrast to results for GTPase inhibition, we determined that insufficient dynamin2 was recruited to complete a complete helix when cells were treated with MiTMAB (Fig. S3 F). This result suggests a role for the PH domain in dynamin helix formation.

Previously, extremely dim and transient bursts of dynamin2 recruitment during early stages of CME were observed in cells overexpressing dynamin2 (Taylor et al., 2011; Aguet et al., 2013). To date, the significance of these events remains unknown, as does the contribution of protein overexpression to the occurrence of these events. Under native expression, we did not observe stable dynamin2 recruitment before 20 s after clathrin appearance, but we did observe rare and transient recruitment events before the stable dynamin recruitment during the late stages of CME (Fig. S1 D). These early, transient events may represent abortive dynamin2 recruitment to CCPs. If this interpretation is correct, recruitment of dynamin below a certain threshold concentration is predicted to be insufficient for stable dynamin2 recruitment.

To test this hypothesis, we depleted DNM2-GFP using siRNAs against dynamin2, and sorted the cells by fluorescence-activated cell sorting (FACS) into two subpopulations based on the intracellular dynamin2 concentration: cells showing either moderate or low dynamin2 expression (i.e., the measured GFP intensity directly reflects the level of dynamin2 expression; Fig. 3 A). When dynamin2 was expressed at the lowest levels, we observed that dynamin2 punctae appeared in exceedingly short bursts, most of which existed for only 1–2 acquisition frames (2–4 s; Fig. 3, B, C, and H). We observed that these bursts represent only to 2–4 dynamin molecules (Fig. 3, F and I). This behavior is similar to the infrequent dynamin2 short bursts observed under normal conditions (Fig. S1 D). Therefore, our results indicate that dynamin2 stable recruitment, but not targeting, is dependent of its own concentration. However, as observed in dynamin knockout cells (Ferguson et al., 2009), the low concentration of dynamin2 did not abolish or prevent CCS formation (Fig. 3 B). Interestingly, we observed that upon moderate dynamin2 depletion, both clathrin and dynamin lifetimes were extended, but dynamin2 was still recruited and remained stably at the CCSs (Fig. 3 B). We determined that in such cases only ∼13 ± 3 dynamin2 molecules were recruited (Fig. 3, E and I). Our data suggest that the early dynamin2 bursts may represent abortive attempts to form stable dynamin2 rings, and that stable dynamin2 assembly in later stages of CME requires passage of a threshold for the local number of dynamin2s recruited.

Actin is an integral component of the CME machinery

Many lines of evidence point to coordination between dynamin and actin function during CME. However, detection of actin at endocytic sites by live-cell imaging has been inconsistent. As a result, whether actin is an integral component of the CME machinery, or only contributes to distinct subpopulations of CCPs, remains unclear. Importantly, the roles for actin in dynamin functions remain incompletely understood. In previous studies, actin recruitment during CME was examined by use of overexpressed fluorescent actin, F-actin probes, or by microinjection of fluorescent G-actin. Therefore, perturbation of actin dynamics and increased fluorescence background might have confounded attempts at actin detection. Interestingly, recent correlative light-electron microscopy results suggested that the frequency of actin recruitment might be underestimated by light microscopy (Collins et al., 2011). Moreover, dynamin2 and actin have not yet been visualized simultaneously in real time.

We therefore sought to quantitatively analyze the dynamic interplay between actin and dynamin2. Zinc-finger nucleases (ZFNs) that target the 5′ terminus of the β-actin gene (ACTB) were designed and used in previously genome-edited SK-MEL-2 cells bearing either CLTA-RFP (SK-MEL-2 hCLTA^{EN-1}) or DNM2-GFP (hDNM2^{EN-1}; Doyon et al., 2011). We generated two cell lines, hCLTA^{EN}/hACTB^{EN} and hDNM2^{EN}/hACTB^{EN}, in which one ACTB allele was tagged with TagGFP or TagRFP-t, respectively (Fig. 4, A and B; and Fig. S5, A and B). As expected, hACTB^{EN} cells displayed fluorescent structures that colocalized with phalloidin-stained stress fibers and actin-rich lamellipodia (Fig. S5 A). This result demonstrates that the fluorescent ACTB is readily incorporated into a variety of actin structures without detectably perturbing them. In fixed cells, the fluorescent ACTB colocalized with phalloidin cortical punctae, and a subset of CLTA-RFP and DNM2-GFP punctae (Fig. 4 B and Fig. S5 B). Interestingly, by editing hACTB^{EN}/hCLTA^{EN} in the U2OS cell line, we observed that clathrin structures typically are linearly organized in a pattern distinct from that seen in the SK-MEL-2 cell line (Fig. S5, B and C). We observed that these CCPs are often distributed along actin stress fibers but also appear in cortical actin punctae like those seen in SK-MEL-2 cells. This observation provides further support for a strong association between clathrin and actin structures. We next sought to elucidate the precise timing and extent of actin recruitment at endocytic sites using live-cell TIRF microscopy.

Analysis of DNM2-GFP and ACTB-RFP dynamics in the genome-edited SK-MEL-2 cells showed that actin polymerization overlaps with dynamin2 recruitment (Fig. 4, B–D). Strikingly, we observed that nearly all dynamin-containing endocytic events (87 ± 1.6%) displayed RFP-ACTB recruitment, demonstrating that actin is an integral component of dynamin-associated endocytic events (Fig. 4, E and F). We further analyzed the dynamics of these events and observed that the timing of actin assembly at endocytic sites is somewhat variable relative to dynamin recruitment. Nonetheless, RFP-ACTB preceded DNM2-GFP in the majority (∼60%) of recruitment events (Fig. 4 G). This observation,

Time = 2 s/frame. Bar, 5 µm. (d–f) Average DNM2-GFP molecule recruitment (±SD) profiles showing number of molecules as a function of time for cells subjected to varying degrees of dynamin depletion in an all-DNM2 allele GFP-tagged SK-MEL-2 cell line (n = 15, 17, 22). (g) Overlay of profiles in d–f. Green indicates control, blue moderate, and red severe knockdown conditions. (h) Average DNM2-GFP lifetime (±SEM) in control, moderate, or severe DNM2-GFP knockdown conditions (n = 3,386, 1,519, 1,704; 9 cells) from CLTA- and DNM2-edited cell line. (i) Average of maximum DNM2-GFP molecules recruited (±SD) in control, moderate, or severe DNM2-GFP knockdown conditions (n = 15, 17, 22).

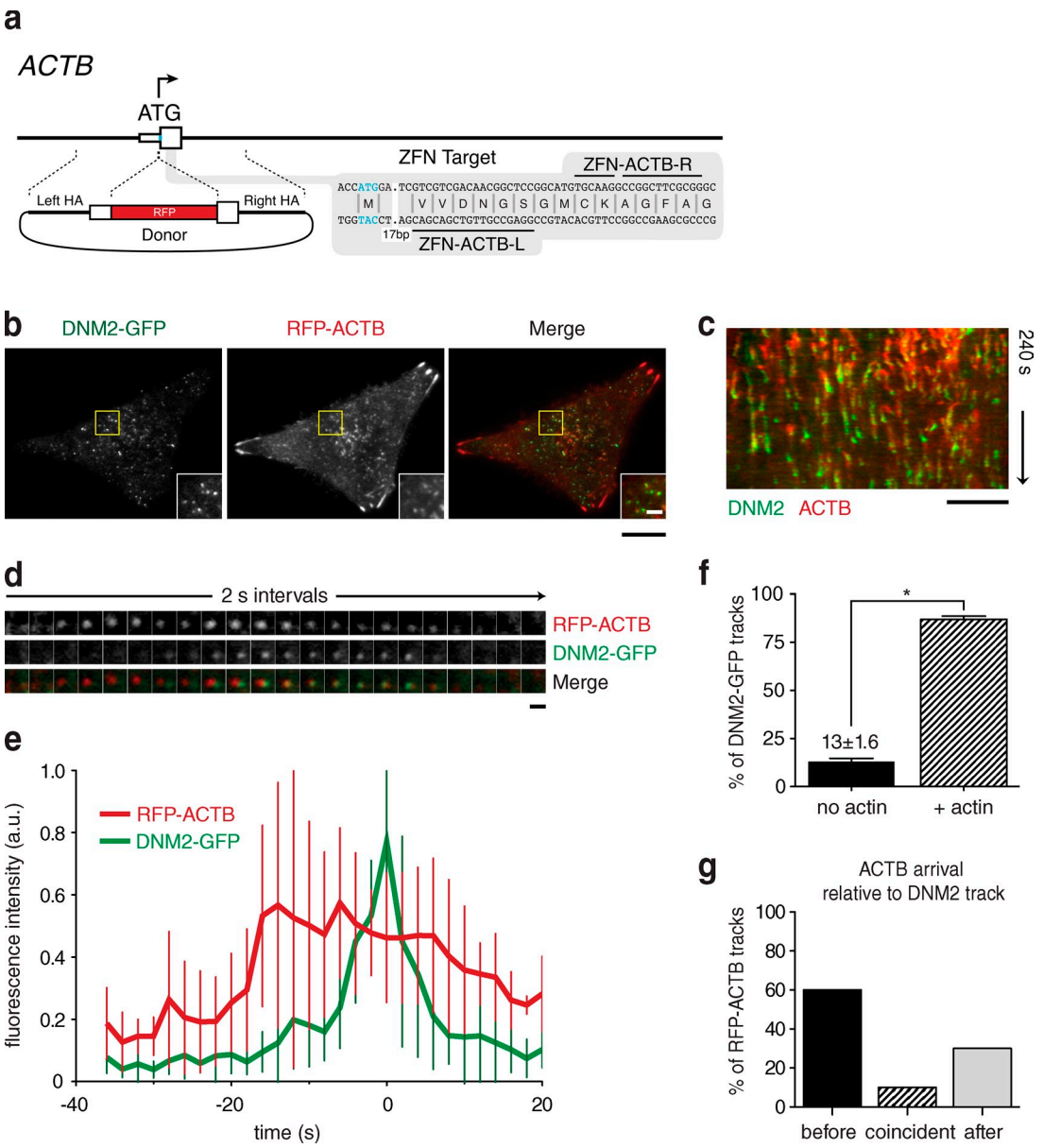

Figure 4. **Actin dynamics in genome-edited SK-MEL-2 cells.** (a) Schematic overview depicting the targeting strategy for integration of Tag-RFP-t (RFP) at the β-actin (ACTB) genomic locus. White boxes represent ACTB exons. HA, donor plasmid region of homology to ACTB sequence. Blue letters, start codon. (b) TIRF microscopy image of a representative SK-MEL-2 hDNM2/hACTB^{EN} cell expressing both DNM2-GFP and RFP-ACTB. Yellow box defines inset. Bars: (main panels) 10 µm; (insets) 2 µm. (c) Representative kymograph depicting endocytic events with dynamin-GFP (in green) and RFP-ACTB (in red). Bar, 5 µm. (d) Representative montage of an endocytic event. Bar, 1 µm. (e) Average DNM2-GFP and RFP-ACTB fluorescence intensity (±SD) profile (tracks = 10; 3 cells). (f) Percentage of DNM2-GFP punctae (±SEM) displaying RFP-ACTB recruitment (number of tracks analyzed = 645; $n = 3$ cells; *, $P < 0.0001$). (g) Percentage of RFP-ACTB (±SEM) punctae arriving before, coincident, or after DNM2-GFP arrival (number of tracks analyzed = 100; $n = 3$ cells).

made without overexpressing any proteins, supports the conclusions that actin acts during multiple steps of CME and that its action is tightly linked with dynamin function.

Interplay between actin dynamics and dynamin2 recruitment and function during CME

We next sought to examine the functional interplay between actin and dynamin2 during CME. Due to the transient nature of the appearance of actin and dynamin2 together at endocytic sites, we developed a similar approach to that used recently by Taylor et al. (2012). In their studies, clathrin dynamics and scission events were examined before, during, and after latrunculin A treatment to inhibit actin assembly. Their studies indicated that actin assembly promotes scission efficiency, similar to conclusions from studies of yeast (Aghamohammadzadeh and Ayscough, 2009; Kishimoto et al., 2011). However, that study focused only on productive events (scission events). Here, by taking advantage of the two-color hCLTA^{EN}/hDNM2^{EN} genome-edited cell line, we were able to perform a complementary unbiased investigation to measure the influence of actin dynamics on all dynamin events.

Addition of the F-actin–stabilizing drug jasplakinolide (1 µM) to cells resulted in an immediate (2–4 s) and dramatic

decrease in the fluorescence intensity of DNM2-GFP membrane punctae (Fig. 5, A and B; and Fig. S5, G–J). Consistent with previous reports, clathrin punctae lifetimes increased dramatically, suggesting a stalling of CCP progression (Fig. 5, A and B; Yarar et al., 2005; Boulant et al., 2011; Taylor et al., 2012). Analysis of DNM2-GFP membrane punctae after drug exposure also revealed a global increase in dynamin lifetimes (Fig. 5, A and E). Moreover, the number of dynamin2 punctae per unit membrane area decreased (by 63%), which is likely due, at least in part, to an observed significant decrease (66% reduction) in the frequency of DNM2-GFP appearance at CME sites (Fig. 5, B–D). By measuring the kinetics of dynamin2 recruitment, we observed that the rate of assembly/recruitment was slower as compared with the control condition (Fig. 5, F and G). However, an approximately similar level of dynamin2 was ultimately recruited after a significantly longer time than in untreated cells (Fig. 5 F). We also observed a lower slope for dynamin2 departure, which suggests perturbation of the dynamin2 scission efficiency, as was observed by Taylor et al. (2012) (Fig. 5 G). The slower recruitment kinetics could explain the overall lower dynamin intensity. Our results indicate that actin plays an important role in the recruitment of dynamin2.

Interestingly, in contrast to jasplakinolide treatment, exposure of cells to drugs such as latrunculin A (Fig. 5 H) or cytochalasin D (CytoD; Fig. S5, D–F) that block actin polymerization caused a rapid stabilization of dynamin2 at endocytic sites (Fig. 5 H). We determined that approximately similar numbers of dynamin2 molecules were eventually recruited before the dynamin2 disassembled (Fig. 5 I). The rates of both recruitment and departure were reduced (Fig. 5 J). By varying the drug concentration, we observed that this effect is dose dependent (Fig. 5 H and Fig. S5, D and E). Together, these experiments demonstrate that actin dynamics have multiple effects on dynamin during the late stages of CME. First, F-actin participates in the initial dynamin recruitment. Because actin assembly can precede dynamin recruitment, it is likely that actin acts indirectly on dynamin at this stage. Upon inhibition of actin polymerization, the persistence of dynamin2 after it reaches its normal concentration at endocytic sites indicates that actin polymerization participates in vesicle scission with dynamin2.

Discussion

In this study we used quantitative fluorescence microscopy to examine the dynamics and functional interplay between clathrin, dynamin2, and actin, all expressed at native levels in cell lines constructed using genome-editing technology. Clathrin lifetimes were variable, just as they are in yeast, but our results also revealed high regularity during the last ∼20 s of CME, which is also similar to budding yeast. This temporal sequence is most often defined by stable recruitment of ∼26 molecules of dynamin2, providing the capacity to form a single loop around the vesicle neck. This step is preceded by transient, irregular recruitment events of 2–4 dynamin2 molecules. Second, we showed that actin is an integral component of the CME machinery and that its assembly usually precedes dynamin2 recruitment. Finally, our results also indicate that F-actin plays three separate functions during CME (Fig. 6). First, F-actin participates indirectly in the initial dynamin2 recruitment. Second, its interplay with dynamin2 regulates the final, robust dynamin2 assembly, and lastly, F-actin promotes vesicle scission.

Clathrin lifetime heterogeneity, CME productivity, and organization

By studying the dynamics of clathrin at the plasma membrane, several groups have observed high heterogeneity in clathrin lifetime (Ehrlich et al., 2004; Merrifield et al., 2005; Yarar et al., 2005; Loerke et al., 2009; Boulant et al., 2011; Banerjee et al., 2012; Taylor et al., 2012). In the present study, we confirmed that even when clathrin is expressed at native levels, its dynamics are characterized by considerable heterogeneity. The significance and the origin of clathrin heterogeneity remain open questions. Previously, a subpopulation of clathrin punctae characterized by short lifetimes (<20 s) was observed. Several lines of evidence suggested that these events might not be productive (Loerke et al., 2009; Taylor et al., 2011). In the present study, we tested this hypothesis by analyzing the recruitment of dynamin2, one of the best-studied factors involved in vesicle scission, to clathrin structures of different lifetimes. Our findings support the conclusion that endocytic sites must mature sufficiently in order to proceed irreversibly toward vesicle formation. This conclusion is congruent with the proposal that some ill-defined minimum threshold (e.g., clathrin assembly, cargo recruitment, etc.) must be satisfied to avoid termination of CME. During the preparation of this manuscript, an independent analysis using our cell line reached similar conclusions, strengthening the proposal that a CCP assembly checkpoint may exist (Aguet et al., 2013).

Roles and recruitment of dynamin2 during CME

Most studies investigating dynamin dynamics during CME relied on overexpression of the neuronal dynamin1 isoform in nonneural cells, and assumed that dynamin1 and dynamin2 act similarly during CME. However, accumulating evidence suggests that the different dynamin isoforms have divergent functional properties (Altschuler et al., 1998; Soulet et al., 2006; Liu et al., 2008). As a result, our understanding of dynamin regulation during CME has been limited. There is a crucial need to examine the function and dynamics of the correct dynamin isoform under unperturbed conditions. In the present study, our analysis focused on the dynamics of dynamin2 expressed at endogenous levels. In the SK-MEL-2 cell line, we could detect dynamin1 mRNA but not protein by RT-PCR and immunoblotting, respectively (Fig. S2). From this analysis, we conclude that dynamin2 molecules outnumber dynamin1 in SK-MEL-2 cells by greater than 70-fold. In the future it will be important to explore simultaneously the native dynamics of dynamin1, dynamin2, and dynamin3 in appropriate cellular contexts.

Dynamin domain functions have been intensively investigated, but the mechanisms governing dynamin2 recruitment to CME sites remain poorly understood. In the present study, we observed that the timing of stable dynamin2 recruitment during CME correlates well with clathrin lifetime (stable recruitment

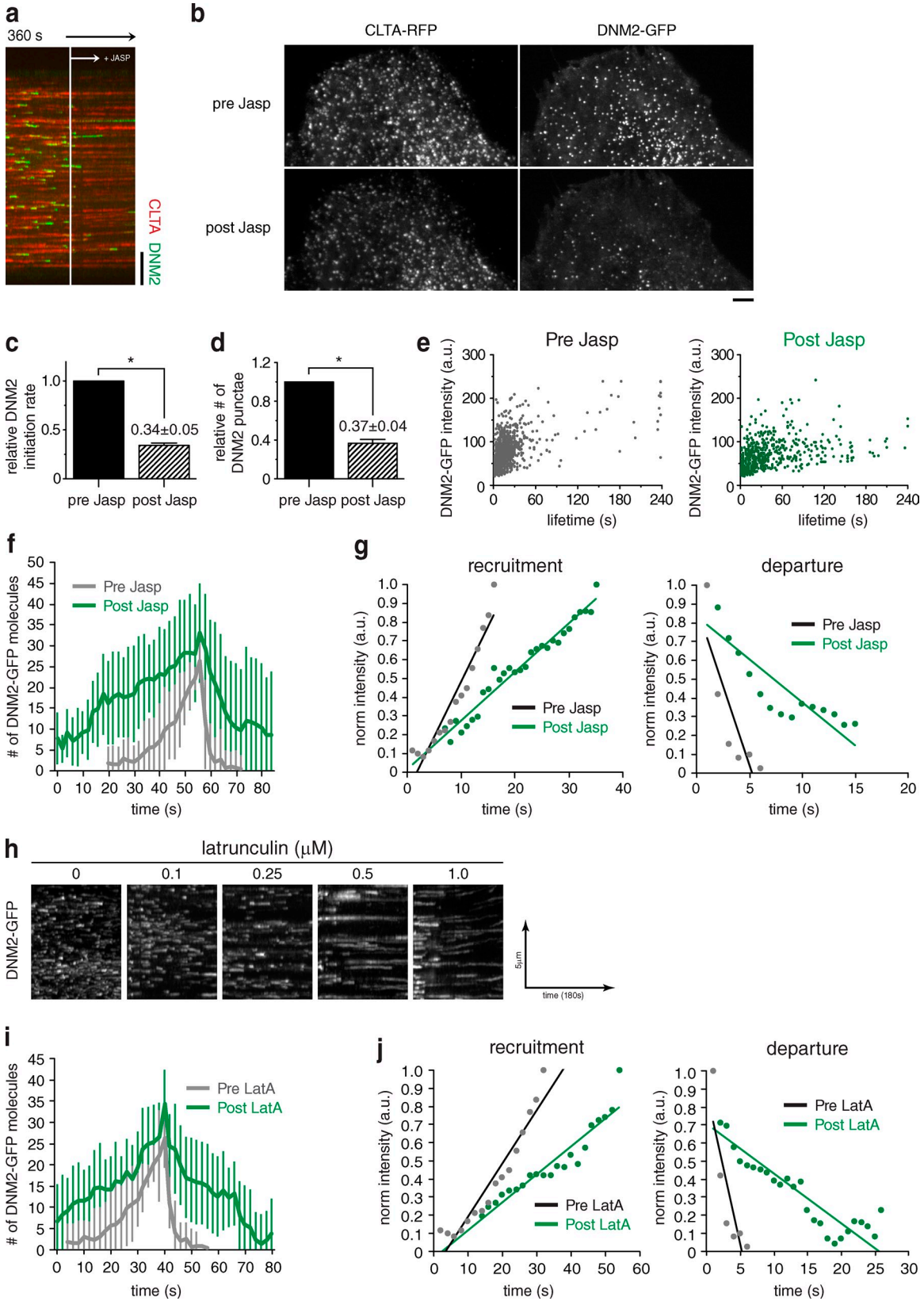

Figure 5. **Effects of actin inhibitors on dynamin kinetics.** (a and b) Representative TIRF microscopy kymograph analysis (a; time = 2 s/pixel, 360 s total) and maximum intensity projection of fluorescence over time, and (b) of a SK-MEL-2 hCLTA^{EN}/hDNM2^{EN} cell subjected to acute 1 μM jasplakinolide exposure. White line in panel a marks time of drug addition. A maximum intensity projection of fluorescence intensity over time (b; of imaging duration = 120 s) was generated for each condition ending or beginning 30 s before or after drug exposure, respectively. Number of punctae analyzed = 323 and 245, respectively. Bars: (a) 5 μm; (b) 2 μm. (c) Relative number of DNM2-GFP membrane punctae (±SEM), both dim and bright, before and after 1 μM jasplakinolide exposure (number of punctae analyzed = 369 and 134, respectively; *n* = 3 cells; *, P = 0.0005). (d) Relative DNM2-GFP initiation

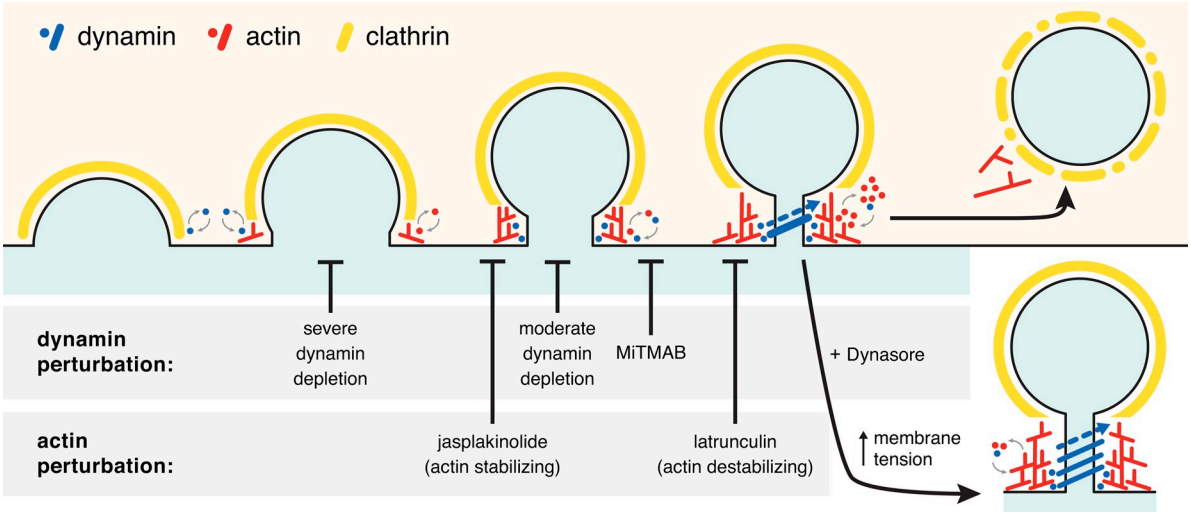

Figure 6. **Model for dynamin2 and actin dynamics and interplay during clathrin-mediated endocytosis.** Points in the pathway affected by dynamin or actin perturbation are indicated.

of dynamin2 occurs ~20 s before vesicle scission irrespective of clathrin lifetime). Previous studies reported that small amounts of dynamin1 could be detected early during CME (Taylor et al., 2011, 2012). Here, we showed that short dynamin2 bursts represent 2–4 molecules, which can be detected for dynamin2 expressed at endogenous levels. By varying dynamin2 levels, we observed that a minimum threshold of dynamin concentration is necessary for its stable recruitment. These early, irregular recruitment events likely represent abortive dynamin recruitment to CME sites (Fig. 6). Our data suggest that the stable dynamin2 recruitment reflects passage through some sort of ill-defined transition point during CME. The conditions that favor dynamin2 recruitment to a critical concentration required for stable assembly need to be explored further. Because dynamin2's PH domain is not required for initial recruitment, it is likely that the recruitment timing for dynamin2 is dependent on its local concentration and on the state of the CCP.

In addition to the well-described dynamin2 role in vesicle scission and CCP maturation, it has been proposed that dynamin might also control an early CME checkpoint (Loerke et al., 2009). In this regard, our results indicate that the rapid and irregular recruitment of 2–4 dynamin molecules could regulate CCP maturation. Once the CCP is mature, dynamin could be further and stably recruited at the neck of the vesicle. Therefore, a minimum dynamin concentration threshold could be in line with this hypothesis. However, this model is not consistent with the observation that CCSs are still formed when dynamin levels are severely reduced. Our results are consistent with those of a previous study, which found that CCPs still form in dynamin KO cells (Ferguson et al., 2009). Finally, the concentration dependence for dynamin stabilization at CCPs could explain why upon overexpression, dynamin2 recruitment can be detected at earlier times and shows prolonged lifetimes (Mattheyses et al., 2011; Taylor et al., 2011). Such observations may have led to erroneous conclusions, which reinforce the importance of maintaining proper stoichiometry of the proteins under investigation.

Much has been learned from in vitro studies of dynamin's scission mechanism, but more work is needed to explore dynamin's scission mechanism in the cellular context with the full complexity of interacting proteins and under physiological conditions. Recent structural studies provided information on the detailed molecular organization of the dynamin assembly, and indicated that dimerization of the dynamin G domain occurs only upon completion of one turn of the helix (Faelber et al., 2011). Considering that formation of a ring around the vesicle neck is proposed to be sufficient to stimulate the GTPase activity, these results indicate that assembly of enough dynamins to encircle the neck may be sufficient to trigger scission. Here, we determined that during CME in live cells typically only 26 dynamin2 molecules are recruited to the vesicle neck, which is sufficient to form a short helix that encircles the neck once. Because CCPs extend away from the plasma membrane, it is possible that TIRF illumination might contribute

rate (±SEM) before and after 1 µM jasplakinolide exposure (number of tracks analyzed = 1,150 and 450, respectively; *n* = 3 cells; *, P = 0.0001). (e) Maximum fluorescence intensity/lifetime dot plot for DNM2-GFP tracks before and after 1 µM jasplakinolide exposure. Each dot represents a single DNM2 track (number of tracks analyzed = 1,017 and 641, respectively). Imaging began 180 s before drug addition, and terminated 180 s after drug addition. Tracks existing within these time frames (before and after drug addition) were analyzed. (f) Average number of DNM2-GFP molecules recruited to endocytic sites as a function of time in cells subjected to 1 µM of jasplakinolide or control conditions (*n* = 15). (g) Slope of DNM2-GFP recruitment and departure in cells subjected to 1 µM of jasplakinolide or control conditions. (h) Representative TIRF microscopy kymograph analysis of DNM2-GFP fluorescence over time in SK-MEL-2 $hCLTA^{EN}/hDNM2^{EN}$ cells exposed to varying concentrations (0–1.0 µM) of latrunculin A actin assembly inhibitor. Drug exposure begins at kymograph start and continues throughout entire kymograph. (i) Average number of DNM2-GFP molecules recruited to endocytic sites as a function of time in cells subjected to 0.1 µM of latrunculin A or control conditions (*n* = 15). (j) Slope of recruitment and departure of DNM2-GFP in cells subjected to 1 µM of jasplakinolide or control conditions (*n* = 15).

to some variation and possibly an underestimate in our dynamin quantification. In the future, it will be important to use additional calibration methods to quantify fluorescently tagged molecules. Interestingly, in a minority of events, sufficient dynamin2 molecules were present to encircle a vesicle neck two or three times. Because in vitro studies have shown that membrane tension can play an important role in scission efficiency (Roux et al., 2006), this observation could reflect a local adaptation of the endocytic machinery. It will be important to explore whether the stoichiometry of others factors is also changed during these events.

CME dynamics and the role of the actin cytoskeleton

For more than 15 years, the role of actin during CME has been investigated and debated, and varied conclusions have been drawn. Several studies found evidence for an actin role during late events (Merrifield et al., 2002; Yarar et al., 2005; Taylor et al., 2012), but depending on the cell type, other studies failed to detect a function for actin during CME. Interestingly, it has also been proposed that actin recruitment to a CME site is dependent on clathrin lifetime (Saffarian et al., 2009). A recent study found evidence that actin assembly at CME sites is necessary when membrane tension is elevated to a certain point (Boulant et al., 2011). However, whether actin assembly at endocytic sites is integral to CME, irrespective of membrane tension, had yet to be determined. To answer this question, we directly investigated the dynamic interplay between dynamin and actin during CME in cells expressing both proteins at native levels. We demonstrated that actin is an integral component of the CME machinery because a burst of actin assembly is observed at essentially all sites of endocytosis. Here, our study focused on the SK-MEL-2 cell line. However, actin has been implicated in different endocytic roles in different cell lines (Fujimoto et al., 2000). To explore such potential variability, we also edited clathrin and actin in the human U2OS cell line (Fig. S5 B). We observed that actin cytoskeleton architecture is markedly different in U2OS versus SK-MEL-2 cells. We observed fewer cortical actin patches corresponding to endocytic sites, but a higher alignment with actin stress fibers, similar to what was observed in HeLa cells (Bennett et al., 2001). It will be important in the future to perform similar analyses in other cell types.

Interestingly, despite the regularity of actin assembly occurring at CME sites, some variability was observed in the relative timing of actin assembly and dynamin recruitment. This variability might reflect modulation of actin polymerization by local membrane tension and/or other factors. However, stable dynamin2 recruitment most often occurred subsequent to actin assembly. This observation indicates that actin can assemble at endocytic sites before and independent of dynamin recruitment. Consistently, in mammalian cells lacking dynamin (derived from a dynamin1/2 double-conditional knockout mouse), CCPs with long tubular necks decorated with actin filaments accumulate (Ferguson et al., 2009). It will be important in the future to determine the mechanism by which actin assembles before dynamin recruitment.

Materials and methods

ZFN design

Enhanced obligate heterodimer ZFNs (55-r975a1-FokI-EL and 56-982a1-FokI-KK) designed to target ±50 bp of the start codon of human ACTB were engineered at Sigma Life Science. ZFNs were prescreened for activity in K562 cells using Surveyor nuclease (CEL-I; Transgenomic) to detect for insertions or deletions (Guschin et al., 2010). In brief, Accuprime Taq HiFi (Invitrogen) was used to amplify a short region surrounding the ZFN target site in a 28-cycle PCR. Resulting amplicons were denatured, slowly re-annealed and treated with Cel-1 for 20 min at 42°C, and then separated on 10% criterion gels (Bio-Rad Laboratories) and visualized by ethidium bromide staining.

Donor design

A donor plasmid carrying Tag-RFP fused to the N terminus of the ACTB gene (Sigma Life Science) was subjected to site-directed mutagenesis by QuikChange (Agilent Technologies). Specifically, to confer increased fluorophore photostability, the Tag-RFP marker was mutated to Tag-RFP-t (see Shaner et al., 2008) by mutation of Tag-RFP amino acid position 162 from serine to threonine (AGC→ACC).

Generation of genome-edited cell lines

ZFN and donor plasmids were transfected into cells using a single-cuvette Nucleofector device (Lonza) as per the manufacturer's protocol. In brief, cells grown to ∼80% confluency were harvested by trypsinization, and 10^6 SK-MEL-2 cells were resuspended in Nucleofector solution R and transfected using Nucleofector program T-020. U2OS cells were resuspended in Nucleofector solution V and transfected using Nucleofector program X-001. After transfection, cells were transferred to 37°C, 5% CO_2. Recovered cells were sorted for RFP-positive or RFP- and GFP-positive signals using a MoFlo high-speed cell sorter (Dako) directly as single cells into 96-well plates.

Cell culture

SK-MEL-2 cell clone Ti13 (hCLTA^{EN-1}/hDNM2^{EN-1} edited) partially tagged, clone Ti20 (hDNM2^{EN-1} edited) partially tagged, and clone Ti95 (hDNM2^{EN-all} edited) all tagged were described previously in Doyon et al. (2011). In brief, ∼1.5 kb of genomic DNA sequence surrounding the CLTA and DNM2 stop codons from SK-MEL-2 cells were amplified using the following primers: SK-MEL-2 CLTA-HA-F, 5′-GGTGGGCTGACCTTGAT-3′; SK-MEL-2 CLTA-HA-R, 5′-TCTATAACCTGTGCTATCCGAG-3′; DNM2-HA-F, 5′-TGTTTGCCAACAGTGACCTC-3′; and DNM2-HA-R, 5′-GTGCAGGGGGTCAGAGAATA-3′. The resulting amplicons were cloned into pCR8-TOPO (Invitrogen) vector and a unique KpnI restriction site was introduced via QuikChange (Agilent Technologies) site-directed mutagenesis with the following primers: SK-MEL-2 CLTA-QC-F, 5′-CAAGCAGGCCCCGCTGGTGCACGGTACCGCCACCCTGTGGAAACACTACATCTGC-3′, SK-MEL-2 CLTA-QC-R, 5′-GCAGATGTAGTGTTTCCACAGGGTGGCGGTACCGTGCACCAGCGGGGCCTGCTTG-3′; DNM2-QC-F, 5′-CCAGCCGAACCATCCCTGCTCGACGGTACCTCGAGGGGGGCGTGCTCT-3′; and DNM2-QC-R, 5′-AGAGCACGCCCCCCTCGAGGTACCGTCGAGCAGGGATGGTTCGGCTGG-3′. Finally, RFP or GFP was amplified using the "KpnI" primers, which encode an N-terminal GTSGGS linker and cloned into the KpnI site of the CLTA or DNM2 homology arm constructs, respectively. SK-MEL-2 and U2OS were maintained under 5% CO_2 at 37°C in DMEM/F12 (Invitrogen) supplemented with 10% FBS (HyClone). SK-MEL-2 cells were used for these studies because of their high transfection efficiency, good and homogenous adherence to glass coverslips, and robust endocytic dynamics.

TIRF microscopy and live-cell imaging

TIRF microscopy images were captured using MetaMorph software on a microscope (model IX-81; Olympus) using an APON 60×/1.49 NA TIRF oil objective and a camera (ORCA-R2; Hamamatsu Photonics). The system was maintained at 37°C using a WeatherStation chamber and temperature controller (Precision Control). At 16–24 h before imaging, cells were seeded onto uncoated glass coverslips in growth medium. During imaging, cells were maintained in DMEM without phenol red (Life Technologies) that was supplemented with 5% FBS (HyClone) and 10 mM Hepes (Life Technologies). A 488-nm solid-state laser (Melles Griot) and a 561-nm diode-pumped solid-state laser (Melles Griot) were used to excite GFP and RFP fluorophores, respectively. For lifetime analysis, images were acquired every 2 s for 3–6 min, with an exposure time of 800 ms. Simultaneous two-color TIRF images were obtained using a DV2 image splitter (MAG Biosystems) to separate GFP and RFP emission signals. Microscopy images

were adjusted for brightness, color balance, and/or contrast uniformly across all pixels, as necessary, in ImageJ (v1.46r; National Institutes of Health). To aid in visualization, microscopy images were enlarged for figures, where necessary, using the "bicubic smoother" interpolation algorithm in Adobe Photoshop (Adobe).

Microscope calibration and single molecule counting
Borosilicate no. 1 coverslips (Corning) were precleaned by three consecutive washes in acetone, 70% ethanol, and Milli-Q water (EMD Millipore). Then, coverslips were further cleaned using oxygen gas plasma for 5 min. Finally, poly-lysine coating was used to functionalize coverslips. Using fluorescent beads and dynamin2-GFP–expressing SK-MEL cells, the 488-nm laser was aligned and the appropriate TIRF angle was determined. Then, purified GFPs (Kerafast) in PBS were directly added to the imaging chamber at a final concentration of 10 ng/ml. After 3 min of incubation, proteins were extensively washed and imaged in PBS. We used an exposure time of 100 ms within the linear range of the camera avoiding any saturation of the camera, allowing rapid acquisition frequency and minimizing photobleaching. No binning was used. A reduced field of acquisition was used, but a similar field of acquisition and position were maintained during an entire imaging session. Images were recorded using a camera (sCMOS Flash 4.0; Hamamatsu Photonics), and a 100×/1.45 NA oil objective (PlanApo; Olympus) was used. For data analysis, we used Icy software to determine the intensity distribution of purified GFP. Spots were detected using a wavelet-based algorithm. For step-bleaching and dynamin2-GFP intensity measurement, we used ImageJ. We drew a 5 × 5-pixel square (312.5 nm × 312.5 nm) centered on the maximum intensity pixel and collected the mean and integrated intensity of the area. To better estimate the intensity due to the protein of interest, purified GFP, or dynamin2-GFP, we performed a background subtraction. We averaged the integrated intensity detected locally (in the same area used for the object detection) during 20 s within at least 30 s between the spot departure or arrival. After transfer to Microsoft Excel, the background value was subtracted from the measured intensity and the number of molecules was determined by dividing the mean measured fluorescent intensity of single-step bleaching of purified GFP.

Drug perturbations
Cells were prepared as described for live-cell imaging. During real-time imaging, a 2–5× concentrated solution of actin drug in DMSO (cytochalasin D; Sigma-Aldrich), jasplakinolide (Sigma-Aldrich), latrunculin A (Sigma-Aldrich), MiTMAB (Abcam), or Dynasore (Sigma-Aldrich) was applied to the cell chamber at a volume of two- to fivefold (in imaging media) over that of the starting imaging media volume.

siRNA-mediated knockdown
The day before transfection, 5.0×10^5 cells were plated into each well of 6-well plates. Transfection was performed using Lipofectamine RNAiMax according to the manufacturer's instructions (Invitrogen). In brief, 5 µl of transfection reagent was mixed with 250 µl of Opti-MEM (Gibco) for 15 min at RT. After incubation, the solution was combined with 200 pmol of siRNA previously diluted in 250 µl Opti-MEM and incubated further for 15 min at room temperature. The combined solution was directly added to each well pre-aliquoted with 1.5 ml of growth media. A nontargeting siRNA pool (siRNA control; ON-TARGETplus SMARTpool siRNA no. 4; Thermo Fisher Scientific) and Silencer Select validated siRNA (5′-ACAUCAACACGAACCAUGA-3′; siRNA ID no. s4212; Life Technologies) against dynamin2 were used for depletion experiments.

Quantitative transferrin uptake assay by fluorescence-activated cell sorting (FACS) analysis
At least 2,000 cells were analyzed for each time point. After 30 min of exposure with DMSO, Dynasore, or MiTMAB, endocytosis was assayed by continuous incubation of 20 µg/ml transferrin conjugated to Alexa Fluor 647 at 37°C for indicated times. Cells were then transferred to ice and surface-bound transferrin–Alexa Fluor 647 was removed using ice-cold acid buffer (DMEM, 0.5% acetic acid and 0.5 M NaCl) for 45 s. The cell culture medium was then neutralized by extensive washes of DMEM-BSA. Cells were collected using EDTA-Trypsin, washed, and fixed in cold 1% PFA. Intracellular fluorescence of transferrin–Alexa Fluor 647 was quantified by FACS (FC500; Beckman Coulter). Results are expressed as a percentage of the intracellular fluorescence measured after 20 min of incubation for controls cells treated with DMSO. Results were normalized to the surface expression of transferrin receptor, evaluated by incubation of the cells with transferrin–Alexa Fluor 647 on ice for 1 h.

FACS of dynamin2 knockdown cells
2 d after siRNA transfection, cells were harvested by trypsinization and FACS sorted using a MoFlo high-speed sorter (Dako). For each depletion condition (moderate or severe), at least 10^5 cells were sorted for GFP intensity. The following criteria were used: (1) moderate depletion group = GFP intensity of ∼20–50% relative to control, and (2) severe depletion group = GFP intensity of ∼0–25% relative to control. Cells were directly seeded onto glass coverslips in 6-well plates, maintained at 37°C, 5% CO_2, and imaged by TIRF microscopy 24 h after sorting (72 h after transfection).

Immunofluorescence and fluorescence staining of fixed cells
Cells were grown on glass coverslips in 6-well plates overnight before fixation in 4% paraformaldehyde at room temperature for 20 min. After three washes with PBS, the coverslips were quenched with 1 mg/ml $NaBH_4$ for 15 min twice, and the cells were permeabilized in 0.1% saponin/PBS or 0.1% Triton X-100/PBS. After brief washing with PBS, the coverslips were incubated with Alexa Fluor 350– or Alexa Fluor 568–conjugated phalloidin (Molecular Probes) at a 1:1,000 dilution for 2 h at room temperature. For immunofluorescence, cells were stained with anti-AP2 (mouse AP6 antibody; Abcam) or anti-HA (mouse 12CA5; Roche) at a 1:1,000 dilution for 1 h. Appropriate secondary antibody coupled to Alexa Fluor 568 was used at a 1:1,000 dilution for 45 min. After three washes with PBS or PBS with 0.5% BSA and 0.1% saponin, the coverslips were mounted on glass slides using ProLong Gold Antifade reagent (Invitrogen) or were visualized directly.

Particle detection, tracking, and image analysis
Particle detection and tracking were performed using Imaris 7.1 software (Bitplane). Before particle detection, images were first subjected to background subtraction. The "Spots" module of Imaris was then used to automatically detect point-like particles with an estimated spot diameter of 350 nm (∼3 pixels). After automatic detection, detected spots were filtered based on satisfying minimum "intensity standard deviation" and "quality" control parameters. Only spots with values higher than the set threshold values were considered for analyses. Quality is defined as the intensity at the center of the spot, Gaussian filtered by 3/4 of the spot radius. Appropriate threshold values were confirmed by visual inspection of correct particle detection. To trace objects through sequential frames of time data, a Brownian motion particle-tracking algorithm was applied. A maximum search distance of 350 nm was defined to disallow connections between a spot and a candidate match if the distance between the predicted future position of the spot and the candidate position exceeded the maximum distance. A gap-closing algorithm was also implemented to link track segment ends to track segment starts to recover punctae that were interrupted by the temporary disappearance of particles. The maximum permissible gap length was set equal to seven frames. Track outputs were then visually inspected and, as necessary, edited to correct for tracking errors. Only punctae that appeared and disappeared during the lifetime of the acquisition (i.e., 181 frames, 6 min) were subjected to lifetime analyses.

Statistical analysis
Paired or unpaired two-tailed *t* tests were used to assess for significance. All tests were performed using Prism (GraphPad Software) and data are presented as mean ± SEM, unless otherwise indicated. All experiments were repeated at least twice, unless otherwise explicitly stated in the figure legends.

Online supplemental material
Fig. S1 shows the variability in dynamin2 recruitment during CME. Fig. S2 presents RT-PCR and Western blot analysis of dynamin isoforms in the SK-MEL-2 cell line. Fig. S3 contains an analysis of dynamin2 recruitment and function during CME in cells exposed to dynamin inhibitors. Fig. S4 shows the effect of dynamin PH* overexpression on dynamin localization and the effect of dynamin inhibitors on AP2 localization and actin cytoskeleton organization. Fig. S5 shows actin localization in genome-edited SK-MEL-2 and U2OS cell lines, the effect of cytochalasin D on dynamin2 dynamics, and the effects of jasplakinolide on dynamin2 and the actin cytoskeleton. Online supplemental material is available at http://www.jcb.org/cgi/content/full/jcb.201403041/DC1.

We thank Fyodor Urnov of Sangamo BioSciences for introducing the Berkeley and Sigma teams. We thank Ann Fisher of the UC Berkeley Cell Culture Facility for help with cell culture. We thank Steve Ruzin of the Biological Imaging Facility, CNR-UC Berkeley, for help with imaging analysis. We thank Hector Nolla, Alma Valero, and Dr. Kartoosh Heydari of the Cancer Research Lab

Flow Cytometry Core Facility of UC Berkeley. We thank Jay T. Groves and Hiroyuki Kai for help with coverslip cleaning. We thank Mark A. Lemmon for providing dynamin mutant plasmids. We thank Jackie Cheng, Christa Cortesio, and Daphne Dambournet for advice and comments on the manuscript.

This work was supported by a California Institute for Regenerative Medicine Predoctoral Fellowship to A.T. Cheng, and by National Institutes of Health grant RO1 GM65462 to D.G. Drubin.

The authors declare no competing financial interests.

Submitted: 11 March 2014
Accepted: 5 May 2014

References

Aghamohammadzadeh, S., and K.R. Ayscough. 2009. Differential requirements for actin during yeast and mammalian endocytosis. *Nat. Cell Biol.* 11:1039–1042. http://dx.doi.org/10.1038/ncb1918

Aguet, F., C.N. Antonescu, M. Mettlen, S.L. Schmid, and G. Danuser. 2013. Advances in analysis of low signal-to-noise images link dynamin and AP2 to the functions of an endocytic checkpoint. *Dev. Cell*. 26:279–291. http://dx.doi.org/10.1016/j.devcel.2013.06.019

Altschuler, Y., S.M. Barbas, L.J. Terlecky, K. Tang, S. Hardy, K.E. Mostov, and S.L. Schmid. 1998. Redundant and distinct functions for dynamin-1 and dynamin-2 isoforms. *J. Cell Biol.* 143:1871–1881. http://dx.doi.org/10.1083/jcb.143.7.1871

Banerjee, A., A. Berezhkovskii, and R. Nossal. 2012. Stochastic model of clathrin-coated pit assembly. *Biophys. J.* 102:2725–2730. http://dx.doi.org/10.1016/j.bpj.2012.05.010

Bennett, E.M., C.Y. Chen, A.E. Engqvist-Goldstein, D.G. Drubin, and F.M. Brodsky. 2001. Clathrin hub expression dissociates the actin-binding protein Hip1R from coated pits and disrupts their alignment with the actin cytoskeleton. *Traffic*. 2:851–858. http://dx.doi.org/10.1034/j.1600-0854.2001.21114.x

Bethoney, K.A., M.C. King, J.E. Hinshaw, E.M. Ostap, and M.A. Lemmon. 2009. A possible effector role for the pleckstrin homology (PH) domain of dynamin. *Proc. Natl. Acad. Sci. USA*. 106:13359–13364. http://dx.doi.org/10.1073/pnas.0906945106

Boulant, S., C. Kural, J.C. Zeeh, F. Ubelmann, and T. Kirchhausen. 2011. Actin dynamics counteract membrane tension during clathrin-mediated endocytosis. *Nat. Cell Biol.* 13:1124–1131. http://dx.doi.org/10.1038/ncb2307

Chappie, J.S., J.A. Mears, S. Fang, M. Leonard, S.L. Schmid, R.A. Milligan, J.E. Hinshaw, and F. Dyda. 2011. A pseudoatomic model of the dynamin polymer identifies a hydrolysis-dependent powerstroke. *Cell*. 147:209–222. http://dx.doi.org/10.1016/j.cell.2011.09.003

Cocucci, E., F. Aguet, S. Boulant, and T. Kirchhausen. 2012. The first five seconds in the life of a clathrin-coated pit. *Cell*. 150:495–507. http://dx.doi.org/10.1016/j.cell.2012.05.047

Collins, A., A. Warrington, K.A. Taylor, and T. Svitkina. 2011. Structural organization of the actin cytoskeleton at sites of clathrin-mediated endocytosis. *Curr. Biol.* 21:1167–1175. http://dx.doi.org/10.1016/j.cub.2011.05.048

Damke, H., D.D. Binns, H. Ueda, S.L. Schmid, and T. Baba. 2001. Dynamin GTPase domain mutants block endocytic vesicle formation at morphologically distinct stages. *Mol. Biol. Cell*. 12:2578–2589. http://dx.doi.org/10.1091/mbc.12.9.2578

Doyon, J.B., B. Zeitler, J. Cheng, A.T. Cheng, J.M. Cherone, Y. Santiago, A.H. Lee, T.D. Vo, Y. Doyon, J.C. Miller, et al. 2011. Rapid and efficient clathrin-mediated endocytosis revealed in genome-edited mammalian cells. *Nat. Cell Biol.* 13:331–337. http://dx.doi.org/10.1038/ncb2175

Ehrlich, M., W. Boll, A. Van Oijen, R. Hariharan, K. Chandran, M.L. Nibert, and T. Kirchhausen. 2004. Endocytosis by random initiation and stabilization of clathrin-coated pits. *Cell*. 118:591–605. http://dx.doi.org/10.1016/j.cell.2004.08.017

Faelber, K., Y. Posor, S. Gao, M. Held, Y. Roske, D. Schulze, V. Haucke, F. Noé, and O. Daumke. 2011. Crystal structure of nucleotide-free dynamin. *Nature*. 477:556–560. http://dx.doi.org/10.1038/nature10369

Ferguson, S.M., and P. De Camilli. 2012. Dynamin, a membrane-remodelling GTPase. *Nat. Rev. Mol. Cell Biol.* 13:75–88.

Ferguson, S.M., A. Raimondi, S. Paradise, H. Shen, K. Mesaki, A. Ferguson, O. Destaing, G. Ko, J. Takasaki, O. Cremona, et al. 2009. Coordinated actions of actin and BAR proteins upstream of dynamin at endocytic clathrin-coated pits. *Dev. Cell*. 17:811–822. http://dx.doi.org/10.1016/j.devcel.2009.11.005

Fish, K.N., S.L. Schmid, and H. Damke. 2000. Evidence that dynamin-2 functions as a signal-transducing GTPase. *J. Cell Biol.* 150:145–154. http://dx.doi.org/10.1083/jcb.150.1.145

Fujimoto, L.M., R. Roth, J.E. Heuser, and S.L. Schmid. 2000. Actin assembly plays a variable, but not obligatory role in receptor-mediated endocytosis in mammalian cells. *Traffic*. 1:161–171. http://dx.doi.org/10.1034/j.1600-0854.2000.010208.x

Gaidarov, I., F. Santini, R.A. Warren, and J.H. Keen. 1999. Spatial control of coated-pit dynamics in living cells. *Nat. Cell Biol.* 1:1–7.

Gibson, T.J., M. Seiler, and R.A. Veitia. 2013. The transience of transient overexpression. *Nat. Methods*. 10:715–721. http://dx.doi.org/10.1038/nmeth.2534

Guschin, D.Y., A.J. Waite, G.E. Katibah, J.C. Miller, M.C. Holmes, and E.J. Rebar. 2010. A rapid and general assay for monitoring endogenous gene modification. *Methods Mol. Biol*. 649:247–256. http://dx.doi.org/10.1007/978-1-60761-753-2_15

Hinshaw, J.E., and S.L. Schmid. 1995. Dynamin self-assembles into rings suggesting a mechanism for coated vesicle budding. *Nature*. 374:190–192. http://dx.doi.org/10.1038/374190a0

Kaksonen, M., C.P. Toret, and D.G. Drubin. 2005. A modular design for the clathrin- and actin-mediated endocytosis machinery. *Cell*. 123:305–320. http://dx.doi.org/10.1016/j.cell.2005.09.024

Kishimoto, T., Y. Sun, C. Buser, J. Liu, A. Michelot, and D.G. Drubin. 2011. Determinants of endocytic membrane geometry, stability, and scission. *Proc. Natl. Acad. Sci. USA*. 108:E979–E988. http://dx.doi.org/10.1073/pnas.1113413108

Lamaze, C., L.M. Fujimoto, H.L. Yin, and S.L. Schmid. 1997. The actin cytoskeleton is required for receptor-mediated endocytosis in mammalian cells. *J. Biol. Chem.* 272:20332–20335. http://dx.doi.org/10.1074/jbc.272.33.20332

Liu, Y.W., M.C. Surka, T. Schroeter, V. Lukiyanchuk, and S.L. Schmid. 2008. Isoform and splice-variant specific functions of dynamin-2 revealed by analysis of conditional knock-out cells. *Mol. Biol. Cell*. 19:5347–5359. http://dx.doi.org/10.1091/mbc.E08-08-0890

Loerke, D., M. Mettlen, D. Yarar, K. Jaqaman, H. Jaqaman, G. Danuser, and S.L. Schmid. 2009. Cargo and dynamin regulate clathrin-coated pit maturation. *PLoS Biol.* 7:e57. http://dx.doi.org/10.1371/journal.pbio.1000057

Macia, E., M. Ehrlich, R. Massol, E. Boucrot, C. Brunner, and T. Kirchhausen. 2006. Dynasore, a cell-permeable inhibitor of dynamin. *Dev. Cell*. 10:839–850. http://dx.doi.org/10.1016/j.devcel.2006.04.002

Mattheyses, A.L., C.E. Atkinson, and S.M. Simon. 2011. Imaging single endocytic events reveals diversity in clathrin, dynamin and vesicle dynamics. *Traffic*. 12:1394–1406. http://dx.doi.org/10.1111/j.1600-0854.2011.01235.x

McMahon, H.T., and E. Boucrot. 2011. Molecular mechanism and physiological functions of clathrin-mediated endocytosis. *Nat. Rev. Mol. Cell Biol.* 12:517–533. http://dx.doi.org/10.1038/nrm3151

Menon, M., and D.A. Schafer. 2013. Dynamin: expanding its scope to the cytoskeleton. *Int Rev Cell Mol Biol*. 302:187–219. http://dx.doi.org/10.1016/B978-0-12-407699-0.00003-0

Merrifield, C.J., M.E. Feldman, L. Wan, and W. Almers. 2002. Imaging actin and dynamin recruitment during invagination of single clathrin-coated pits. *Nat. Cell Biol.* 4:691–698. http://dx.doi.org/10.1038/ncb837

Merrifield, C.J., D. Perrais, and D. Zenisek. 2005. Coupling between clathrin-coated-pit invagination, cortactin recruitment, and membrane scission observed in live cells. *Cell*. 121:593–606. http://dx.doi.org/10.1016/j.cell.2005.03.015

Morlot, S., and A. Roux. 2013. Mechanics of dynamin-mediated membrane fission. *Annu Rev Biophys*. 42:629–649. http://dx.doi.org/10.1146/annurev-biophys-050511-102247

Park, R.J., H. Shen, L. Liu, X. Liu, S.M. Ferguson, and P. De Camilli. 2013. Dynamin triple knockout cells reveal off target effects of commonly used dynamin inhibitors. *J. Cell Sci.* 126:5305–5312. http://dx.doi.org/10.1242/jcs.138578

Quan, A., A.B. McGeachie, D.J. Keating, E.M. van Dam, J. Rusak, N. Chau, C.S. Malladi, C. Chen, A. McCluskey, M.A. Cousin, and P.J. Robinson. 2007. Myristyl trimethyl ammonium bromide and octadecyl trimethyl ammonium bromide are surface-active small molecule dynamin inhibitors that block endocytosis mediated by dynamin I or dynamin II. *Mol. Pharmacol.* 72:1425–1439. http://dx.doi.org/10.1124/mol.107.034207

Roux, A., K. Uyhazi, A. Frost, and P. De Camilli. 2006. GTP-dependent twisting of dynamin implicates constriction and tension in membrane fission. *Nature*. 441:528–531. http://dx.doi.org/10.1038/nature04718

Saffarian, S., E. Cocucci, and T. Kirchhausen. 2009. Distinct dynamics of endocytic clathrin-coated pits and coated plaques. *PLoS Biol.* 7:e1000191. http://dx.doi.org/10.1371/journal.pbio.1000191

Sever, S., H. Damke, and S.L. Schmid. 2000. Dynamin:GTP controls the formation of constricted coated pits, the rate limiting step in clathrin-mediated endocytosis. *J. Cell Biol.* 150:1137–1148. http://dx.doi.org/10.1083/jcb.150.5.1137

Shaner, N.C., M.Z. Lin, M.R. McKeown, P.A. Steinbach, K.L. Hazelwood, M.W. Davidson, and R.Y. Tsien. 2008. Improving the photostability of bright

monomeric orange and red fluorescent proteins. *Nat. Methods*. 5:545–551. http://dx.doi.org/10.1038/nmeth.1209

Sirotkin, V., J. Berro, K. Macmillan, L. Zhao, and T.D. Pollard. 2010. Quantitative analysis of the mechanism of endocytic actin patch assembly and disassembly in fission yeast. *Mol. Biol. Cell*. 21:2894–2904. http://dx.doi.org/10.1091/mbc.E10-02-0157

Soulet, F., D. Yarar, M. Leonard, and S.L. Schmid. 2005. SNX9 regulates dynamin assembly and is required for efficient clathrin-mediated endocytosis. *Mol. Biol. Cell*. 16:2058–2067. http://dx.doi.org/10.1091/mbc.E04-11-1016

Soulet, F., S.L. Schmid, and H. Damke. 2006. Domain requirements for an endocytosis-independent, isoform-specific function of dynamin-2. *Exp. Cell Res.* 312:3539–3545. http://dx.doi.org/10.1016/j.yexcr.2006.07.018

Takei, K., P.S. McPherson, S.L. Schmid, and P. De Camilli. 1995. Tubular membrane invaginations coated by dynamin rings are induced by GTP-gamma S in nerve terminals. *Nature*. 374:186–190. http://dx.doi.org/10.1038/374186a0

Taylor, M.J., D. Perrais, and C.J. Merrifield. 2011. A high precision survey of the molecular dynamics of mammalian clathrin-mediated endocytosis. *PLoS Biol.* 9:e1000604. http://dx.doi.org/10.1371/journal.pbio.1000604

Taylor, M.J., M. Lampe, and C.J. Merrifield. 2012. A feedback loop between dynamin and actin recruitment during clathrin-mediated endocytosis. *PLoS Biol.* 10:e1001302. http://dx.doi.org/10.1371/journal.pbio.1001302

Wu, J.Q., and T.D. Pollard. 2005. Counting cytokinesis proteins globally and locally in fission yeast. *Science*. 310:310–314. http://dx.doi.org/10.1126/science.1113230

Yarar, D., C.M. Waterman-Storer, and S.L. Schmid. 2005. A dynamic actin cytoskeleton functions at multiple stages of clathrin-mediated endocytosis. *Mol. Biol. Cell*. 16:964–975. http://dx.doi.org/10.1091/mbc.E04-09-0774